Continuum modeling of projectile impact and penetration in dry granular media

Continuum Modeling of Projectile Impact with Dry Granular Media

Sachith Dunatunga and Ken Kamrin

Abstract

Modeling of impact into granular substrates is a topic of growing interest over the last decade. We present a fully continuum approach for this problem, which is shown to capture an array of experimentally observed behavior with regard to the intruder penetration dynamics as well as the flow and stress response of the granular media. The intruder is modeled as a stiff elastic body and the dry granular bulk is modeled using a 'trans-phase' constitutive relation. This relation has an elasto-viscoplastic response with pressure- and rate-sensitive yield behavior given by the $\mu(I)$ inertial rheology when the granular free volume is below a critical value. Above this critical value, the material is deemed to separate and is treated as a disconnected, stress-free medium. The Material Point Method is used to implement the impact problem numerically. Validations are conducted against a wide set of experimental data with a common granular material, which allows use of a single model calibration to test the agreement. In particular, continuum simulations of projectile impact with different shaped intruders and different impact energies show good agreement with experiments regarding of time-of-flight, penetration depth, and Poncelet drag force coefficients. Simultaneously, good agreement with experiments is found regarding the response of the granular media during impact, such as the pressure wave propagation process during the initial stage of impact, the flow fields that develop under the moving intruder, and the free-surface dynamics.

1 Background

The impact of a solid intruder into a dry granular medium is a problem that has received growing attention in recent years for its many applications (e.g. geological and astrophysical as in Melosh (1989); Furbish et al. (2007); Housen and Holsapple (2003); Holsapple (1993); Zhao et al. (2015)). These systems, as we discuss below, are frequently modeled using reduced-order intrusion models, which provide intruder dynamics but do not solve for the motion of the granular domain, or grain-by-grain discrete element methods (DEM). A broadly accurate continuum approach could be an advantageous methodology for these systems, providing details of both grain dynamics and intruder motion without the cost of DEM. Continuum treatments, especially if they invoke a small set of parameters, could also lead to new analytical tools to shed understanding on the impact process. However, continuum modeling of impact comes with many theoretical and numerical challenges. Granular materials are challenging to model as a continuum, displaying a combination of behaviors from the traditional phases of matter (gas, liquid, solid) depending on load and packing conditions. During an impact, these phases can all appear simultaneously — zones farther from the intruder behave as a stiff elastic material, zones surrounding the intruder undergo high levels of dense plastic flow, and at the free surface the material becomes loose and splashes before settling into a post-impact, possibly cratered configuration. Given a constitutive model capable of accurately representing the different phases, to compute solutions one would also need a versatile solver able to calculate solid elastic response, extreme plastic deformations, and large nominally stress-free volumetric expansions with accuracy. It must permit an element of material to undergo transitions between these phases and for the granular body to undergo topological changes as the intruder embeds and is enveloped by the grains. The contact interaction with the intruding body brings added challenges, particularly if the intruding body cannot be considered as a rigid or elastic solid.

Several other approaches may be considered to solve this class of problems. Traditionally, aside from experiments (Clark, Kondic, and Behringer 2012; Clark and Behringer 2013; Clark, Petersen, and Behringer 2014; Clark et al. 2015; Clark, Kondic, and Behringer 2016), or scaling relations (Newhall and Durian 2003; Bruyn and Walsh 2004), macroscopic force laws on the intruder motion (Allen, Mayfield, and Morrison 1957;

Katsuragi and Durian 2007) have been successfully used to glean insight into the impact process, even from as early as the works of Euler and Poncelet. However, typically these methods are only able to capture specific phenomena, such as trajectories and forces on the intruder, and reveal little about other aspects of the system (e.g. flow fields in the granular bulk).

The discrete element method (DEM), first described in Cundall and Strack (1979), is regarded as one of the most accurate computational tools available for granular systems. DEM achieves this level of accuracy by solving the classical equations of motion on each grain individually; unfortunately, this results in untenable computational expense for problems involving large time spans or with high numbers of grains. A distinct advantage of DEM for simulation of impact of *solid* intruders is that it can account for the intruding bodies in an "automatic" manner – that is, the intruder can simply be considered as a rather large grain with certain material properties and the method itself can remain the same. However, liquid intruders, or those with more complicated constitutive models, may prove difficult in DEM. Despite this, DEM is readily used to model granular impact, as was done in Kondic et al. (2012), and can serve essentially as a tightly controlled experiment, given that the total number of grains remains small enough compared to the computational power and time available. In order to solve problems involving many grains or a long time-scale, it is therefore worth investigating if a unified *continuum* approach can be used to model the entirety of the granular impact process.

Regarding continuum approaches, many constitutive models have been used to various degrees of success in modeling the behavior of granular materials. While the rate-independent Drucker-Prager and Mohr-Coulomb models are generally successful in predicting the onset of plastic deformation, more recent rheological models such as the $\mu(I)$ relation in da Cruz et al. (2005) (extended to 3D in Jop, Forterre, and Pouliquen (2006)) and the nonlocal granular fluidity model (an extension of Jop, Forterre, and Pouliquen (2006)) in Kamrin and Koval (2012) are more accurate in solving problems with zones of dense, rapid flow, where rate-sensitivity and particle size effects can play a stronger role. Although at first glance granular impact may appear to be a highly transient event, recent work from Clark, Kondic, and Behringer (2016) shows that the flow of the granular bulk directly underneath the intruder is well-captured by a dynamic steady-state profile, in which the flow field is self-similar in time and scales linearly with the instantaneous intruder velocity for a majority of the impact process. This suggests that rheological models arising from quasi-steady-state assumptions, such as $\mu(I)$, should in fact be able to replicate the intruder dynamics from these events. Furthermore, if rate-sensitivity is not a large factor here, $\mu(I)$ reduces to a rate-independent model with a Drucker-Prager failure criterion and non-associated flow rule, and it is possible this even simpler model could capture a majority of the intruder dynamics well compared to the full $\mu(I)$ relation.

In addition to the constitutive model, the equations of motion must be solved, and various methods have been proposed, with the division typically between solid methods (largely finite-element derived methods) and fluid methods (various, but largely finite-volume derived methods). While both sets of methods are successful in their respective regimes (e.g. implementation of the $\mu(I)$ rheology in the Navier-Stokes solver Gerris for dense, flowing systems as in Lagrée, Staron, and Popinet (2011); Staron, Lagrée, and Popinet (2012); Staron, Lagrée, and Popinet (2014)), unified modeling of the various granular phases under a single method is difficult and still an active area of research. Granular impact is a good example where all behaviors are present. Deep in the granular bulk the material acts largely as an elastic solid. Near the tip of the intruder the flow is very similar to that of a yield-stress fluid. Furthermore, many grains are ejected near the free surface, resulting in a dilute gas-like phase which may nevertheless be important if ejecta dynamics or the post-impact surface shape and stress fields are desired. Ideally, such a continuum method would also allow seamless use of different constitutive models for both the granular bulk and the intruding body; while in this work we only focus on elastic solid intruders, liquid drops have shown interesting behaviors and have many applications as well (Zhao et al. 2015).

The Material Point Method (MPM), first described in Sulsky, Chen, and Schreyer (1994), combines the strengths of both fluids solvers and the finite element method. It allows for large inhomogeneous deformation and topological changes while supporting elasticity, true yield functions, and complex, history-dependent constitutive models without an interpolation or remeshing step on stress or state variables. The earlier particle-in-cell (PIC) method (Harlow 1964) and the fluid-implicit-particle (FLIP) method (Brackbill, Kothe, and Ruppel 1988) directly precede MPM, but were generally not applied to solid mechanical problems. In MPM, the state of a continuous body is saved at Lagrangian material points, but the equations of motion are solved on an ephemeral background mesh in a manner analogous to an updated Lagrangian FEM step.

As the material points contain the entire state of the simulation, the mesh can be reset at the beginning of each time step, allowing for large deformations to accumulate on material points without any particular mesh deforming excessively. The ability of MPM to seamlessly allow topological changes (as the connectivity between material points is not fixed) is of particular relevance to impact-type problems, as the bulk granular material may both create new surfaces and merge existing ones during the impact process. These attractive properties have allowed other practitioners to use MPM in saturated soil problems with large deformations (Abe, Soga, and Bandara 2013; Bandara and Soga 2015), granular flow in silos (Więckowski 2003; Więckowski 2004; Więckowski and Kowalska-Kubsik 2011), granular column collapse problems (Andersen and Andersen 2009; Mast et al. 2015), and even wedge indentation in soft soils (Farias, Llano-Serna, and Nairn 2012). However, the constitutive models used in these works typically do not handle possible tensile stress states, and either ignore the dilute gas-like phase which results, or assume that all extensile deformation can be subsumed as plastic dilation even as densities drop below the limit for contact connectivity.

Variants of MPM have been developed to address shortcomings of the original method, typically at the expense of increased computation. Many of these variants involve improving the integration techniques when obtaining coefficients for the system of equations necessary to solve the equations of motion, the first of which was termed the Generalized Interpolation Material Point Method (GIMP) in Bardenhagen and Kober (2004). As GIMP spreads the influence of the material point, the computational cost is inceased by a small factor (depending on dimensionality) from that of the original formulation, but in turn can help reduce problems present in the original form, such as cell-crossing error. Further improvements and practical forms for extension to three dimensional problems were shown in the Convected Particle Domain Interpolation (CPDI) method in Sadeghirad, Brannon, and Burghardt (2011) and CPDI2 in Sadeghirad, Brannon, and Guilkey (2013), which remarkably have no extra computational cost over GIMP in one and two dimensions, provided that the deformation gradient (or material point corner locations in CPDI2) is tracked on each material point. Finally, the original implementation in Sulsky, Chen, and Schreyer (1994) only allows no-slip contact between separate bodies; contact algorithms have been developed to address this shortcoming, such as that of Bardenhagen et al. (2001) and Huang et al. (2011). Although experimental evidence and the collisional model in Clark, Petersen, and Behringer (2014) suggest that the value of surface friction between the intruder and the bulk granular medium is largely unimportant, using an improved contact algorithm allows us to vary this parameter, or even simulate entirely frictionless contact between the intruder and the bulk.

The current work builds upon the constitutive/numerical approach in Dunatunga and Kamrin (2015) to show that dry granular impact processes can be well-represented with a single, unified granular continuum model. The results also serve as the first comprehensive validation of this 'trans-phase' modeling framework, which had previously only been tested for individual scalings (e.g. chute flow shows the Bagnold profile, silos show Beverloo scaling, etc.). The experiments that we compare against all utilize the same granular media, which reduces fitting to provide a more stringent test of the modeling. Even though the impact process spans dynamic and static behaviors, the continuum model is shown to work in a variety of impact conditions, and many relevant aspects of the problem can be extracted from a single simulation once the appropriate material constants are known. Specifically, we show that penetration depths and times are reproduced for many intruder shapes and energies, as are the Poncelet-type drag-force functions often used to model intruder dynamics. The granular flow under the intruder is also in agreement with experiments, confirming the presence of a steady-state normalized velocity profile. Thanks to the experiments in Clark et al. (2015), we are also able to validate the model's elastodynamic predictions, comparing against data for force propagation during the initial stage of impact. Additionally, the deformation and spallation of the free-surface is qualitatively well-matched with discrete element simulations. To implement the impact simulations numerically, we enhance our previous MPM procedure to permit higher-order accuracy in the spatial integration and to allow multi-body frictional contact between separate continuous bodies.

2 Theory

The constitutive framework is related to the model introduced in Dunatunga and Kamrin (2015). Throughout, we use the notation for continuum mechanics defined in Gurtin, Fried, and Anand (2010). The spatial gradient and spatial divergence operators are given by grad and div respectively, while material time deriva-

tives are represented by an overdot. The transpose of a tensor $\mathbf{A}$ is given by $\mathbf{A}^T$, the trace by $\operatorname{tr}\mathbf{A}$, and the deviator by $\mathbf{A}_0 = \mathbf{A} - \frac{1}{3}(\operatorname{tr}\mathbf{A})\mathbf{I}$ in 3D.

The equation for momentum balance is

$$\operatorname{div}\mathbf{T} + \rho\mathbf{b} = \rho\dot{\mathbf{v}}, \tag{1}$$

where the Cauchy stress is denoted by $\mathbf{T}$, ρ is the density, $\mathbf{b}$ is the specific body force, and $\dot{\mathbf{v}}$ is the material rate of change of the velocity. The spatial velocity gradient, spin, and stretching tensors are defined as

$$\mathbf{L} = \operatorname{grad}\mathbf{v}, \qquad \mathbf{W} = \frac{1}{2}(\mathbf{L} - \mathbf{L}^T), \qquad \mathbf{D} = \frac{1}{2}(\mathbf{L} + \mathbf{L}^T), \tag{2}$$

and, by mass balance, the density evolution obeys

$$\dot{\rho} = -\rho \operatorname{tr}\mathbf{L} \tag{3}$$

assuming the motion is smooth (e.g. we are not inside a shock).

From the stress tensor, we define the equivalent shear stress, pressure, and Drucker-Prager stress ratio, respectively, by

$$\bar{\tau} = \sqrt{\frac{1}{2}(\mathbf{T}_0 \colon \mathbf{T}_0)}, \qquad p = -\frac{1}{3}\operatorname{tr}\mathbf{T}, \qquad \mu = \bar{\tau}/p \tag{4}$$

where : denotes the tensorial contraction (defined for tensors $\mathbf{A}$ and $\mathbf{B}$ as $\mathbf{A}\colon\mathbf{B} = \sum_i \sum_j A_{ij}B_{ij}$). Note that the model itself is expressed as a three-dimensional relation; however, the examples shown in this work reduce to the plane-strain case, where $D_{zz} = 0$ but $T_{zz} \neq 0$ in general.

The constitutive relation takes the form of an elasto-viscoplastic relation with pressure-sensitive plastic flow rule, extended to allow transitions to and from a gas-like 'open' material state. Our model employs a hypoelastic-plastic framework. The usual procedure for a hypoelastic-plastic model is to perform an additive decomposition of the velocity gradient into elastic and plastic parts, $\mathbf{L} = \mathbf{L}^e + \mathbf{L}^p$. These elastic and plastic velocity gradients are further decomposed into stretching ($\mathbf{D}^e$ and $\mathbf{D}^p$) and spin ($\mathbf{W}^e$ and $\mathbf{W}^p$) tensors. Unlike the alternative hyperelastic-plastic framework, hypoelastic-plastic models are not derived from an energy potential. However, they avoid reliance on tracking the deformation gradient tensor $\mathbf{F}$, which may become ill-behaved when large, inhomogeneous deformations are applied, as are commonplace in granular flows. Moreover, because the grains themselves are stiff, granular elasticity invokes small elastic stretches, which tends to reduce the issues that may arise in hypoelastic models.

During dense flow, we assume a flow rule of the form $\mathbf{D}^p = \hat{\mathbf{D}}^p(\mathbf{T})$. In the common case of codirectionality (the deviator of the Cauchy stress and the deviator of the plastic stretching are in the same direction) and isochoric (volume-preserving) plastic deformation, we can further write the flow rule as

$$\hat{\mathbf{D}}^p(\mathbf{T}) = \dot{\bar{\gamma}}^p(\mathbf{T})\frac{\mathbf{T}_0}{2\bar{\tau}}, \tag{5}$$

where $\dot{\bar{\gamma}}^p$ is the equivalent plastic shear strain rate. In dense granular flow, codirectionality is approximately satisfied; see DEM simulations of stiff grains by da Cruz et al. (2005); Silbert et al. (2001); Koval et al. (2009). The isochoric assumption is reasonable when the critical state of constant-volume flow is rapidly approached, which is the case, relatively speaking, in problems with high strains and rates. Even so, the packing fraction of dense (non-collisional) granular flows rarely varies by more than a few percent. With these simplifications, the problem reduces to determining $\dot{\bar{\gamma}}^p$ given a stress state $\mathbf{T}$.

For the function $\dot{\bar{\gamma}}^p(\mathbf{T})$ we adopt the '$\mu(I)$ rheology' presented in da Cruz et al. (2005); Jop, Forterre, and Pouliquen (2006). The model is essentially a pressure- and rate-sensitive plasticity relation which relates the stress ratio μ to the inertial number defined by $I = \dot{\bar{\gamma}}^p\sqrt{\frac{d^2\rho_s}{p}}$. The relation is commonly fit to the functional form

$$\mu = \mu(I) = \mu_s + \frac{\mu_2 - \mu_s}{I_0/I + 1} \quad \text{if} \quad I > 0, \quad \text{and} \quad \mu \leq \mu_s \quad \text{if} \quad I = 0, \tag{6}$$

where I_0 is a material constant, ρ_s is the density of solid particles, and d is the mean particle size. We can rewrite this equally as a relation for the flow stress:

$$\bar{\tau} = \bar{\tau}(p, \dot{\bar{\gamma}}^p) = p\left(\mu_s + \frac{\mu_2 - \mu_s}{I_0/\dot{\bar{\gamma}}^p\sqrt{d^2\rho_s/p} + 1}\right) \quad \text{if} \quad \dot{\bar{\gamma}}^p > 0, \quad \text{and} \quad \bar{\tau} \leq p\mu_s \quad \text{if} \quad \dot{\bar{\gamma}}^p = 0. \tag{7}$$

Inspection of this form when considering $\dot{\bar{\gamma}}^p$ shows that no plastic flow can occur if $\mu < \mu_s$, and therefore μ_s is considered a static friction coefficient. The parameter μ_2 serves as an upper limit on the stress-ratio during flow. As plastic transients are neglected (due to the assumption that the expected total shear deformation is large compared to the shear required to reach a "critical state"), our plasticity model is defined solely through equations 5 and 6.

We use an equation of state for the pressure wherein the pressure below a critical density is taken to be zero. Above the critical density we assume a constant bulk modulus. The critical density is set to be the density when volumetric strain is zero. We can write this concisely as

$$K(\rho) = \begin{cases} 0 & \text{if } \rho < \rho_c \\ K_c & \text{if } \rho \geq \rho_c. \end{cases} \tag{8}$$

Here K_c is a constant bulk modulus of dense media (that is, the granular assembly taken as a whole). Physically speaking, we view ρ_c as the density at which the grains are just barely in contact with each other, with vanishingly small force at each contact. Volumetrically expanding a particle system at ρ_c renders the grains separated and *disconnected*; hence the pressure is zero. Compressing a system at ρ_c increases the relative displacements of the contacting particles and likewise increases the contact forces; hence the pressure increases with increasing compression, or equivalently, increasing density. The transition from a dense granular state to the disconnected state can be reconciled as a transition to a low-temperature granular gas (Dunatunga and Kamrin 2015).

Since we use a hypoelastic-plastic model, we must choose an objective rate for the stress evolution equation; we use the Jaumann (corotational) rate, which is given by

$$\overset{\triangle}{\mathbf{T}} \equiv \dot{\mathbf{T}} - \mathbf{W}\mathbf{T} + \mathbf{T}\mathbf{W}. \tag{9}$$

The elasticity is then written as a relation between the elastic stretching $\mathbf{D}^e = \mathbf{D} - \mathbf{D}^p$ and the stress-rate, given by

$$\overset{\triangle}{\mathbf{T}} = \mathbb{C} : \mathbf{D}^e \equiv 2G(\mathbf{D}_0 - \mathbf{D}_0^p) + K\,\mathrm{tr}(\mathbf{D} - \mathbf{D}^p)\mathbf{I} \tag{10}$$

where the fourth-order elastic stiffness tensor, $\mathbb{C}$, is given by $\mathbb{C} = 2G\mathbb{I} + (K - 2G/3)\mathbf{I} \otimes \mathbf{I}$, where $\mathbb{I}$ is the fourth-order identity tensor and the bulk and shear moduli are given by K and G respectively. We also make reference to the Young's modulus, which is given by $E = 9KG/(3K + G)$, and the Poisson ratio, given by $\nu = (3K - 2G)/(6K + 2G)$.

As the material has no stress when in tension and remains essentially stress-free (with the exception of negligible kinetic stresses) until the density returns to the critical value, we call the dilute phase *disconnected*. When the material is at a density higher than the critical density, the grains are in compression (implying a positive pressure), so we can use the $\mu(I)$ rheology and elasticity to compute the stress state, and we term this the *dense* phase. The material response can be expressed universally by

$$\overset{\triangle}{\mathbf{T}} = \mathbb{C}(\rho) : (\mathbf{D} - \hat{\mathbf{D}}^p(\mathbf{T})), \tag{11}$$

where $\mathbb{C}(\rho)$ is given by combining eqs. (8) and (10) and $\hat{\mathbf{D}}^p$ is obtained from eqs. (5) and (7). We refer to the above model as a *trans-phase* constitutive relation — it reduces to solid elasticity when $\rho \geq \rho_c$ and $\mu < \mu_c$, it gives fluid-like plastic flow when $\rho \geq \rho_c$ and $\mu \geq \mu_c$, and it gives a gas-like disconnected granular behavior when $\rho < \rho_c$. Although here we only consider an elastic response that is linear, data from Clark et al. (2015), to which we will compare our model later, show some evidence of nonlinear elastic behavior in their material composed of discs. This would go beyond the nominally linear response obtained from Hertzian interactions

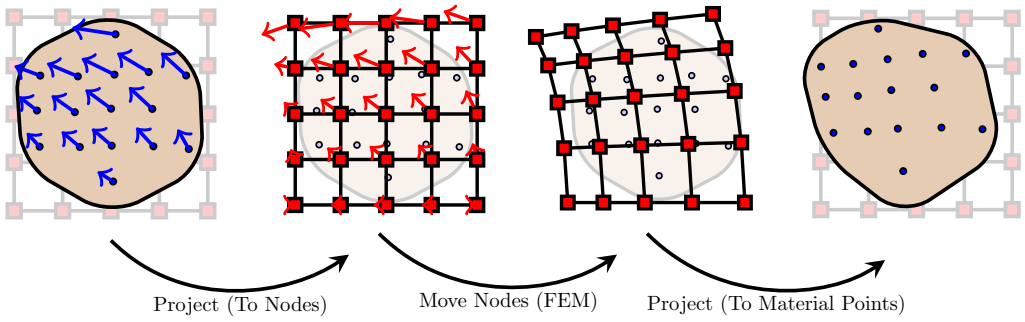

Figure 1: A single MPM step. First material point data (blue circles) is projected onto a background mesh (red squares). An explicit finite element step is then run to obtain the background mesh deformation. Finally, these deformations are projected onto the material points, which then update their states (such as position and stress), and the mesh is reset for the next time step. We stress that the points drawn represent material points of the continuum; they are not individual grains.

of contacting disks. If deemed necessary, nonlinear elasticity could be incorporated in our model through the choice of the $\mathbb{C}(\rho)$ relation above ρ_c, in order to incorporate the desired dependence of the bulk modulus on density. A nonlinear elastic model might be more essential in materials composed of spheres rather than disks, where Hertzian contact has a nonlinear power law.

3 Method

The material point method is used for the underlying numerical method, which solves the equations of motion and provides the velocity gradient for the constitutive model. In MPM the stress, momentum, and mass are stored and updated on a set of Lagrangian material points. One time-step of MPM updates the positions of the materials points and the quantities stored on them. To do so, each step the method introduces a background finite-element mesh; herein we exclusively use a cartesian mesh of linear elements. The physical quantities stored on the material points are projected onto the nodes of the mesh and then a single finite-element step is conducted, which uses momentum balance and constitutive information to move the mesh and update the nodal quantities. The finite-element solution is projected from the mesh back onto the material points, giving the points new positions and updated values for the physical quantities stored on them. This marks the end of the procedure for one time-step. Note that the distorted finite-element mesh is never referred to again as the next step begins anew with an undistorted mesh. In so doing, issues of large mesh distortion do not arise in MPM even though large strains may be occurring on the material points. See fig. 1 for a flow chart of the MPM update procedure.

3.1 Integration

To maintain accuracy and manage computational expense in the impact simulations, we use an augmentation to the original version of the material point method by Sulsky, Chen, and Schreyer (1994). The original method makes use of a delta function idealization of particle influence during integration. This assumption is computationally efficient as integrals are then simply single function evaluations, however undesirable effects such as cell-crossing error can appear in this formulation. Fundamentally, these effects stem from neglecting the spatial extent of the material point influence when performing the integration. However, in practice, we find that many of these effects are mitigated or diminished by a sufficiently small time step. In Dunatunga and Kamrin (2015), the problems investigated did not require high levels of geometric refinement; however, with the current set of simulations, geometry plays a crucial role in our investigations, and we need to ensure that this geometry is correctly captured. Using a similar Courant–Friedrichs–Lewy (CFL) number (which gives a necessary condition for stability on the time step size given the elastic wave speed) as in the previous simulations would have resulted in large computational expense, as relatively speaking more particles and

elements are present than in prior work. Addressing the integration issue allows us to increase the CFL number relative to that which is stable for the simpler delta function formulation, overall resulting in less computational expense.

As an example, for first order elements in one dimension, we have shape functions and gradients given by

$$S_i(x) = \max\left[0, (1 - \frac{1}{\Delta x}|x_i - x|)\right] \tag{12}$$

$$\nabla S_i(x) = \begin{cases} \frac{1}{\Delta x}\operatorname{sgn}(x_i - x) & \text{if } |x_i - x| \leq \Delta x \\ 0 & \text{otherwise} \end{cases} \tag{13}$$

respectively, where x_i is the position of the node and Δx is the grid spacing (higher dimensional shape functions can be generated from products of the one dimensional functions). Using the delta function approximation, the elements of the sparse mapping matrices used to project to and from the nodes to the material points, are

$$S_{ip} = S_i(x_p), \quad \nabla S_{ip} = \nabla S_i(x_p), \tag{14}$$

where x_p is the position of the material point. However, particularly for the estimation of the gradient, there are issues with the delta function idealization, mainly near element boundaries – in one dimension, we can see that the gradient is constant, up until the point where the material point crosses the node. Then, the sign of the gradient switches abruptly; if we consider that particle stresses are mapped to nodal forces through this gradient operator, we see that this results in the force rapidly changing sign as a material point crosses a node, which can lead to nonphysical artifacts.

It is this cell-crossing error which can be largely mitigated through considering the spatial extent of the material point when computing the gradient. Later MPM variants such as the Generalized Interpolation Material Point Method (GIMP) from Bardenhagen and Kober (2004) and Convected Particle Domain Interpolation (CPDI) from Sadeghirad, Brannon, and Burghardt (2011) are capable of performing a more accurate integration by reconsidering the numerical extent of the material point (in the case of GIMP, via choosing the appropriate particle characteristic functions). It is important to distinguish the numerical and physical extents of the material points; these methods concern only the numerical extent. For details on this distinction, we refer to Sadeghirad, Brannon, and Guilkey (2013). The numerical extent is used to spread the influence of material points and to obtain better estimates, in particular for the gradients, over the delta function formulation. This is done by sampling the shape function at multiple points instead of analytically differentiating the piecewise function (and later assuming the derivative is constant instead of examining each section separately). The physical extent is the actual material subdomain that a material point is supposed to represent. It may have a complex, difficult-to-integrate shape (we do not track this shape entirely, only its scalar volume). In one dimension, CPDI improves accuracy by evaluating the shape function at the left and right corners of the particle numerical domain and dividing by the particle size to estimate the gradient (this ensures that the gradient approaches zero as the material point approaches nodes, allowing a smooth transition), and the approach in the cited works can be generalized to higher dimensions. That is, in one dimension, we can write the elements of the mapping matrices as

$$S_{ip} = (S_i(x_p^L) + S_i(x_p^R))/2, \quad \nabla S_{ip} = (S_i(x_p^R) - S_i(x_p^L))/(x_p^R - x_p^L), \tag{15}$$

where x_p^L and x_p^R are the left and right corners of the numerical extent of the material point. While this results in a minor increase in computational cost, the improved integration increases accuracy and minimizes cell-crossing effects.

Due to the tremendous strains which may occur in granular flows, especially in the impact/penetration/splash problem, we wished to avoid reliance on the deformation gradient $\mathbf{F}$ when determining the numerical domain of a material point's influence. Unfortunately, the first version of CPDI uses the deformation gradient to update the particle extent – the second version, presented in Sadeghirad, Brannon, and Guilkey (2013), does not need to utilize $\mathbf{F}$ as it advects material point corners with the displacement field, however we did not implement this version as it can suffer issues similar to Finite Element mesh tangling (e.g. when Jacobians become singular). While we chose to retain the CPDI framework, we disabled the extent updates through $\mathbf{F}$. One may choose to let only $\det \mathbf{F}$ change the material point numerical extent through isotropic dilation

and contraction. However, the volume changes experienced by the granular material while in the gas phase can be extremely large, which, if distributed isotropically, can in turn lead to non-physical effects such as the corners of a material point becoming embedded deep inside the bulk. Instead, for the current work, we opt to use a fixed material point extent with a predefined finite volume, analogous to uGIMP (Bardenhagen and Kober 2004; Sadeghirad, Brannon, and Burghardt 2011). This middle-ground solution relieves the grid-crossing error to permit lower CFL numbers, but without posing heavy-handed assumptions on material point influence in highly expanding regions. Note that although the extent used to approximate the integration does not change, we do update the physical volume of the material point using the density via Eq 3. This physical volume is used to weight the approximated integrals so the appropriate quantities (e.g. masses and forces) are correctly projected onto the grid nodes and vice-versa.

3.2 Contact

By default, the material point method allows for multiple bodies to interact only through a no-slip contact condition. Although we are able to run simulations with this contact condition, the deformation immediately underneath the intruder appears nonphysical, as bulk material is unable to flow around the intruder and instead "piles up" in a single element ahead of it.

The contact algorithm presented in Huang et al. (2011) is a further refinement of the one developed in Bardenhagen et al. (2001). A minor modification was needed as the algorithm presented is given for the Update Stress First formulation of MPM, while we use the Update Stress Last form; simply, we do not need to break up the algorithm into two phases (before and after the stress update step), and can instead just run the entire contact algorithm before the stress update step. There is additional computational expense compared to the no-slip MPM algorithm (which is achieved "for free" in the default formulation), as a separate background grid must be created for each object and forces must be computed where separate grids disagree on nodal velocity. However, the cost is minor unless the simulations are particularly sparse or the contact surface is extremely large.

There is notable visual qualitative improvement when using the contact algorithm rather than default no-slip; particularly, the pileup effect is eliminated and material is able to flow around the intruder as we physically expect. With this algorithm, we are also able to modify the surface friction coefficient between the bulk and intruder – in practice, we found that although no surface friction (perfect slip, $\mu_{\text{surf}} = 0$) appeared qualitatively different than even a small amount of surface friction ($\mu_{\text{surf}} = 0.05$), increasing the surface friction even up to the the bulk coefficient of friction, μ_s, did not significantly alter results further. This is consistent with the collisional model in Clark, Petersen, and Behringer (2014). Unsurprisingly, the perfect-slip simulations displayed greater sensitivity to the initial conditions; for this reason, we used a surface friction of $\mu_{\text{surf}} = 0.1$ in all of our simulations presented, as the intruder is a relatively smooth object but certainly has a few imperfections which preclude perfect slip.

3.3 Overview

With the exception of the improvements in the integration and contact algorithm noted above, the overall MPM procedure takes a standard form. We still retain the use of the explicit dynamic integration due to the phenomena of interest present in the impact process, including the propagation of stress waves, and we continue to use the update stress last variant.

Recalling that the mapping matrices S_{ip} and ∇S_{ip} are no longer single point evaluations, mapping material point quantities to nodes at the beginning of a step remains

$$m_i^n = \sum_p S_{ip} m_p, \qquad (m\mathbf{v})_i^n = \sum_p S_{ip} m_p \mathbf{v}_p^n, \qquad \mathbf{b}_i^n = \sum_p S_{ip} m_p \mathbf{b}_p^n, \qquad \mathbf{f}_i^n = \sum_p -v_p \mathbf{T}_p^n \cdot \nabla S_{ip}, \tag{16}$$

where m_p is the (constant) particle mass, and $\mathbf{v}_p^n$, $\mathbf{b}_p^n$, and $\mathbf{T}_p^n$ are the particle velocity, specific body force, and Cauchy stress respectively (the n superscript indicates the beginning of the step). The nodal quantities, indexed by i, are given in order as the mass, momentum, body force, and internal forces at the beginning of the time step. If more than one body contributes to particular nodes across meshes, those bodies are considered in contact, so the contact algorithm needs to run on these nodes, which contributes to the nodal

forces. The total nodal force is given by

$$(\dot{m\mathbf{v}})_i^n = \mathbf{b}_i^n + \mathbf{f}_i^n + \mathbf{f}_{\text{contact}}. \tag{17}$$

Once the nodal quantities are produced, nodal momenta are calculated per body using forward Euler integration to yield

$$(m\mathbf{v})_i^{n+1} = (m\mathbf{v})_i^n + \Delta t(\dot{m\mathbf{v}})_i^n. \tag{18}$$

Likewise, since the nodal mass remains constant in a time step, the nodal acceleration and velocity respectively are given by

$$\dot{\mathbf{v}}_i^{n+1} = \frac{(\dot{m\mathbf{v}})_i^n}{m_i}, \qquad \mathbf{v}_i^{n+1} = \frac{(m\mathbf{v})_i^{n+1}}{m_i}. \tag{19}$$

After applying boundary conditions, the nodal kinematic quantities are used to update the material point velocity, velocity gradient, and position through

$$\mathbf{v}_p^{n+1} = \mathbf{v}_p^n + \Delta t \sum_i S_{ip}\dot{\mathbf{v}}_i^{n+1}, \qquad \mathbf{L}_p^{n+1} = \sum_i \mathbf{v}_i^{n+1} \otimes \nabla S_{ip}, \qquad \mathbf{x}_p^{n+1} = \mathbf{x}_p^n + \Delta t \sum_i S_{ip}\mathbf{v}_i^{n+1}. \tag{20}$$

Note that since material points only contribute to small subset of nodes (and vice-versa), the sums involved are only over a small portion of the domain (when mapping to particles) or only over a small number of particles (when mapping to nodes). Once the velocity gradient is computed, the trans-phase constitutive relation can be used to update the Cauchy stress at the material points (see implicit update routine in Dunatunga and Kamrin (2015)), which then completes the step.

Prior to discussion of our results, we emphasize that this study is mainly concerned with the ability of the numerical method and mathematical model to converge upon the multitude of results observed in experiments; many "low-hanging fruit" are still available in both program and method optimization for the MPM numerics. Nevertheless, we provide our metrics to establish a baseline level of performance, with the caveat that changes may be made that can significantly reduce run time. Nonuniform mesh refinement and nonuniform material point distributions could be used to cut down significantly on both the wall and CPU times in these problems at the expense of additional programming complexity. Parallelization could be used to reduce the wall time for large individual simulations; our implementation has this capability but as we required a large number of relatively coarse simulations compared to a small handful of extremely fine ones, using a single thread per simulation results in greater throughput. Furthermore, an implicit (dynamic) time discretization can save tremendous amounts of computational time (Sulsky and Kaul 2004) by allowing larger time steps to be taken. Together, these changes should result in a much faster MPM solver, but would also require much more programmer time to implement.

4 Results

4.1 Material parameters

Common to all but the very last of the simulations, we wish to simulate the bulk properties of Vishay Precision Group's PS-1 material, which is used in Clark, Kondic, and Behringer (2012); Clark and Behringer (2013); Clark, Petersen, and Behringer (2014); Clark (2014); Clark et al. (2015); Clark, Kondic, and Behringer (2016). A single grain of this material is disc-shaped, has a density of 1.28 $\mathrm{g\,cm^{-3}}$, and has a Young's modulus of 1.28 GPa. We chose the Young's modulus and Poisson ratio for the bulk granular media to be, respectively, $E = 20$ MPa, and $\nu = 0.45$. The values of the elastic material parameters were chosen to be in the general range of the results of the appendix in Clark et al. (2015) and the main text of Bathurst and Rothenburg (1988). We assume that the packing fraction Φ in the dense phase is 0.79, so ρ_c is given by 1.0112 $\mathrm{g\,cm^{-3}}$. Although in reality the material is bidisperse with diameters of 4.3 mm and 6 mm, we set the diameter in the rate-sensitivity for the $\mu(I)$ model to be 5.0 mm. Because the constituents are discs constrained to flow as a 2D granular assembly, our fully-3D formulation is specialized to plane-strain and calibrated so as to match the in-plane mechanical properties of the disk media.

For the important μ_s and μ_2 parameters, direct measurements of these values have not been measured for the material used. Instead, we used knowledge based on prior work for similar disk-based materials, such as Silbert et al. (2001); Kamrin and Koval (2014), to formulate a small range of acceptable values. We initially ran one simulation of penetration depth as a representative sample with a value chosen in this range, and found that the results were indeed close to the experimental observations. We observed some sensitivity to the choice of μ_s, but much less to the choice of μ_2. We chose $\mu_s = 0.320$, $\mu_2 = 0.598$, and $I_0 = 0.278$. No numerical fitting procedure was applied to optimize these choices; this single set of parameters was calibrated once from a single penetration depth example and used for all of the experimental validation tests. Although the value for μ_s seems somewhat low, corresponding to a friction angle of 17.75 degrees, this is indeed consistent with DEM findings utilizing frictional disks, such as Silbert et al. (2001); Kamrin and Koval (2014). The given material properties result in a p-wave speed of 272 m/s in the bulk as estimated from the density and p-wave modulus ($M \equiv E(1-v)/(1-v-2v^2)$). We provide two sets of validations of our constitutive model, corresponding to those concerning intruder dynamics and those concerning the response of the granular bulk.

Note that even though we have used the $\mu(I)$ rheology here, it is interesting to see how closely a simple rate-independent model (such as an elasic-perfectly plastic material with a Drucker-Prager yield criterion and non-associated flow rule) can replicate the intruder motion, given that we observed a much stronger dependence of the results on μ_s than μ_2. Indeed, appendix A shows that the rate-independent model captures the results quite well in this particular configuration, although there are small but noticeable differences at high kinetic energies.

4.2 Intruder

We first investigate an intruder impacting a granular bulk corresponding to the experiments in Clark, Petersen, and Behringer (2014). The intruders have a range of initial kinetic energies as well as shapes. The shapes are distinguished by the slope s of the intruder tip. We specifically compare the final depth, flight time, and two force-related parameters relevant to the model presented in that work.

The mass of each intruder is held to a constant value of 0.219 kg. In the experimental work, the intruder has a density corresponding to that of bronze at $8.91\,\mathrm{g\,cm^{-3}}$. However the thickness of the intruder is 2.2 mm, whereas the thickness of the bulk granular material is 3 mm. Therefore, the average areal density per unit length (in the out-of-plane dimension) of the intruder in our simulation is taken as $6.5\,\mathrm{g\,cm^{-3}}$. We did not note a high degree of sensitivity to the elastic properties of the intruder; choosing a Young's modulus of 40 MPa and poisson ratio of 0.45 did not noticeably alter a few representative results compared to cases where higher elastic moduli were used (up to 1 GPa). To keep the stable time step size as large as possible (and reduce the computational expense), we ran all simulations with the lowest values except when noted otherwise.

We replicated the shapes of the intruders tested in the experimental work, with the exception of the sharp corners; we regularized these for numerical purposes by rounding corners with a radius of 1 cm. Any mass lost due to rounding is added onto the tail section of the intruder to keep the total mass constant. We initially filled elements with four material points per element located at the centers of the element quadrants, although there is some indication from Farias, Llano-Serna, and Nairn (2012) that efficiency may be increased by choosing a different discretization for the intruder. Simulations were run on a cluster composed of Intel Xeon E5645 processors. To maximize total throughput, we ran all simulations in single-threaded mode, which were managed through the use of GNU parallel from Tange (2011). When the cluster was fully loaded, each simulation took approximately 18 hours of wall time to complete, with over 30,000 total material points and a grid size of 100 elements in both the horizontal and vertical directions, for a total of 10,000 elements. However, individual simulations run when the cluster was relatively unloaded measured at well under half that time, with an average time of around 4 hours. Again no parallelization is used here, as total throughput across many simulations was the goal; a single simulation could be run at a faster pace by distributing the work.

The area simulated was a 0.91 m by 0.91 m square, corresponding to the smallest in-plane dimension of the experimental setup. We used a time step size of 3 µs, and simulated up to 0.5 s (although it is clear from the results that simulations are essentially completed by 0.3 s). A sequence of material point distributions from two representative simulations are shown in fig. 2. Interestingly, we note that a single plume is observed

above the intruder (seen at 400 ms in each simulation), which is significant as there is no interstitial fluid in this simulation. This is consistent with the zero-pressure limit of the results found in Royer et al. (2008).

We first checked that the kinematic quantities matched between simulations and experiment. In experiments, Clark, Petersen, and Behringer (2014) measured both the depth an intruder ultimately settled at and the time it took to approach this depth. Results are plotted in fig. 3. We extracted these results from the simulations; the depth is simply the z-displacement of the center of mass of the intruder from the moment it impacts the granular bulk to the end of the simulation. The resting time is non-trivial to define due to elastic oscillations; we plot the last time the z-position of the intruder differed by more than 0.2 percent of the final depth in an effort to prevent small oscillations in position from artificially increasing the resting time. Flight time calculations vary within as much as 0.01 s by changing this threshold from 0.1 to 0.3 percent of the final depth.

We also compared force coefficients obtained from our data assuming that the intruder obeys the differential equation

$$m\ddot{z} = mg - f(z) - h(z)\dot{z}^2. \tag{21}$$

Equation (21) has been studied in relation to granular impact in Clark, Petersen, and Behringer (2014); Clark and Behringer (2013); Clark, Kondic, and Behringer (2012) and the problem has been studied in even earlier works.

In this model, $f(z)$ is the static force which depends on the intruder shape and current depth. The $h(z)$ term is a collisional term, and also depends on the intruder shape and current depth. Note that neither $f(z)$ nor $h(z)$ depend on the velocity of the intruder. Therefore, if we have measurements of $m\ddot{z}$ and $\dot{z}^2$ for multiple initial velocities at the same fixed z position z_k, we can solve a linear least squares problem to obtain estimates of $f(z_k)$ and $h(z_k)$ for a given intruder shape. Repeating this procedure over several distinct z_k allows us to see the behavior of the $f(z)$ and $h(z)$ functions. Note that this corresponds to the first procedure mentioned in Clark and Behringer (2013), which may have a large spread with experimental data, in which case the Kinetic Energy Formulation explained in that work (first developed in Ambroso, Kamien, and Durian (2005)) is more useful as it delays the application of numerical differentiation. However, we found that the results from simulations were amenable to the least-squares procedure. Because we store data for different simulations at the same time, rather than the same z-position, we need to post-process our output data to obtain estimates for the $f(z)$ and $h(z)$ functions. To do this, we first generated a smooth trajectory $z(t)$ through cubic splines of the position data. The function is essentially one-to-one before the intruder comes to a stop, and therefore we used the inverse function to compute the set of t_k for each simulation corresponding to a desired z_k. Differentiating the spline representation of $z(t)$ and evaluating at t_k allowed us to obtain the velocity and acceleration at z_k. Two example spline trajectories as well as their derivatives, with $s = 0.5$ and 1.5 and a common initial velocity of 3.55 $\mathrm{m\,s^{-1}}$ are shown in fig. 2. Note that in this particular case for the $s = 1.5$ intruder, the Kinetic Energy corresponds to appoximately 1.37 J; comparison with the general trend in fig. 3 shows that this experiment had a greater final depth than would be expected by a trend line, resulting in our simulations slightly underestimating the depth for this particular experiment.

We then used the least squares procedure to determine the best estimates for $f(z_k)$ and $h(z_k)$, which yields fig. 4. The weakness of this approach is that the spline is not accurate over the first few depth data points, so we ignored these; similarly, when the $z(t)$ function ceases being one-to-one, we again could not use this procedure to obtain estimates on these coefficients. Increasing the sampling rate of the simulation would help us obtain data at smaller depths and at depths closer to the settling position. In the range of validity, we see both the static term $f(z)$ and the collisional term $h(z)$ match well with the experimental data from Clark, Petersen, and Behringer (2014). The main anomalous result is the ordering of the $s = 0$ curve in the $h(z)$ plot and the much weaker dependence of the shape on the $h(z)$ curves; however, overall the data compares well to experiments.

These experimental works have suggested a local surface-level, collision-based picture to explain the obtained resistance coefficient $h(z)$. The fact that it arises as well from a fully continuum treatment suggests the particle motions assumed in the collisional model, if back-expanded to locations displaced from the intruder tip, might approximate the velocity field we find on a control volume boundary extending in front of the intruder. Flow through such a volume is the key determiner, from a continuum standpoint, for the $h(z)$ function, as it determines the rate of momentum exchange with the intruder.

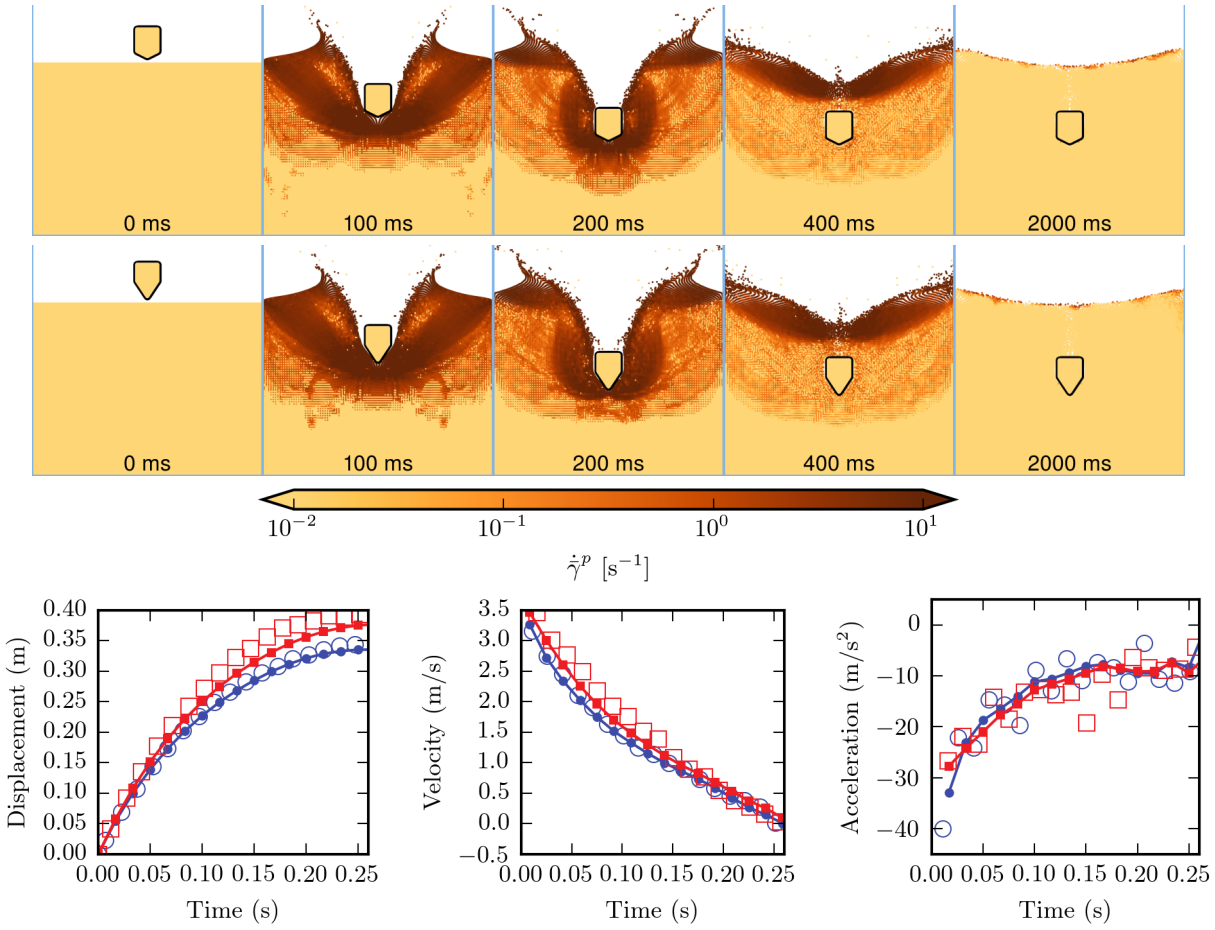

Figure 2: The instantaneous equivalent plastic shear strain rate at multiple stages of the continuum impact simulation for two representative cases: $s = 0.5$ (top) and 1.5 (middle), $v = 3.5$ m s^{-1} common to both. Colors correspond to the magnitude of equivalent plastic shear strain rate in log scale, and are plotted on the material points. The intruder is outlined in black. From left to right: The initial configuration, which is when the intruder is just about to enter the granular bulk, followed by tunneling through, followed by collapse of the top layers forming a central plume, and finally both the intruder and the bulk have come to rest in a static configuration. We show displacement (bottom left), velocity (bottom center), and acceleration (bottom right), generated from displacement data for the same cases ($s = 0.5$ and $s = 1.5$ for a common initial velocity of 3.55 m s^{-1}). The colors and markers follow those of fig. 3.

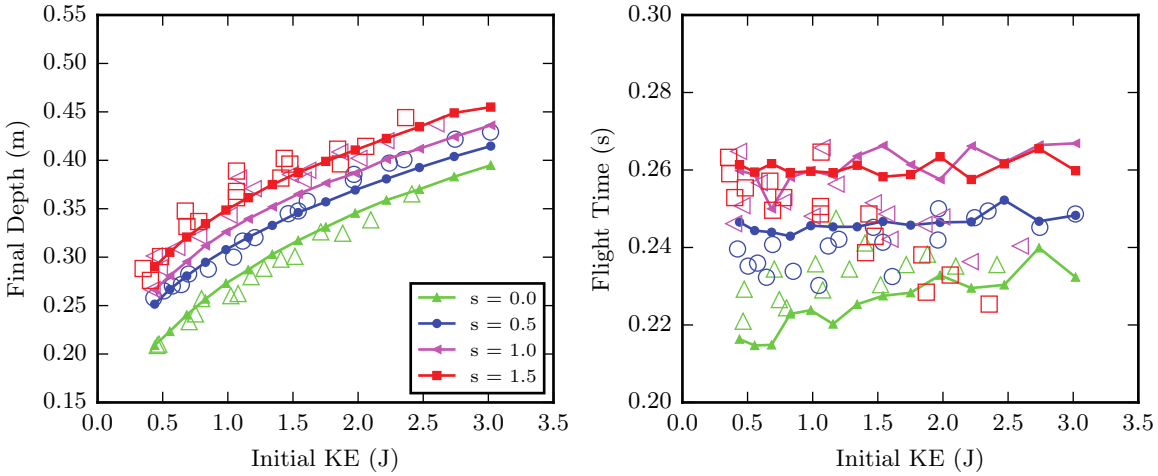

Figure 3: Final depth from the original surface of the bulk material (left) and the time until the intruder comes to a stop (right). Simulation results are represented by closed markers with connecting lines, while experimental results from Clark, Petersen, and Behringer (2014) are shown as open markers with no connecting line (the shape and colors correspond between simulation and experiment). Final depth is taken to be the position at the end of 0.5 s, where all simulations appear to be entirely static. Stopping time calculated as the last time the intruder position is at most 0.2% of the total depth away from the final position.

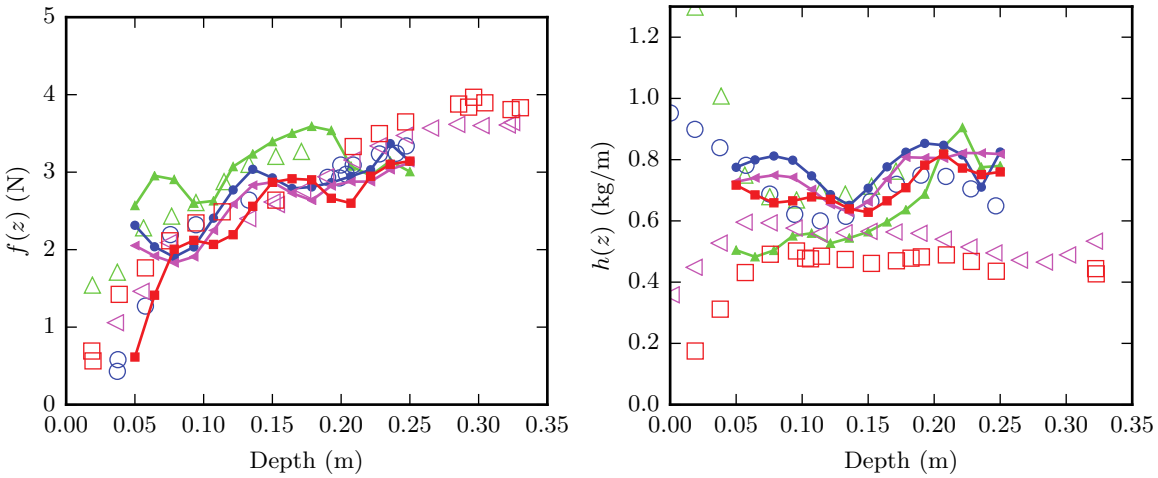

Figure 4: Static force term $f(z)$ (left) and the coefficient of the inertial term $h(z)$ (right) as done in Clark, Petersen, and Behringer (2014). Plotting conventions from fig. 3 are used. The coefficients are obtained through a fitting procedure to the dynamical model proposed in the cited work, as detailed in the main text.

4.3 Granular Bulk

4.3.1 Force Propagation

The intensity plot shown on the left of fig. 5 was created from analysis of a very high resolution simulation focusing on the point of impact between the intruder and the granular bulk. Since the system is essentially hyperbolic at this point, we are able to cut out a large portion of the bulk. The entire intruder is still retained, however, as it is small enough that p-waves can traverse across and reflect multiple times over the course of the simulation – in practice however we did not see much difference from increasing the bulk modulus of the intruder much beyond that of the bulk granular media. As this is an explicit-dynamic scheme, the stability criterion is related to the smallest element size and the stiffest modulus, so it is advantageous to keep the

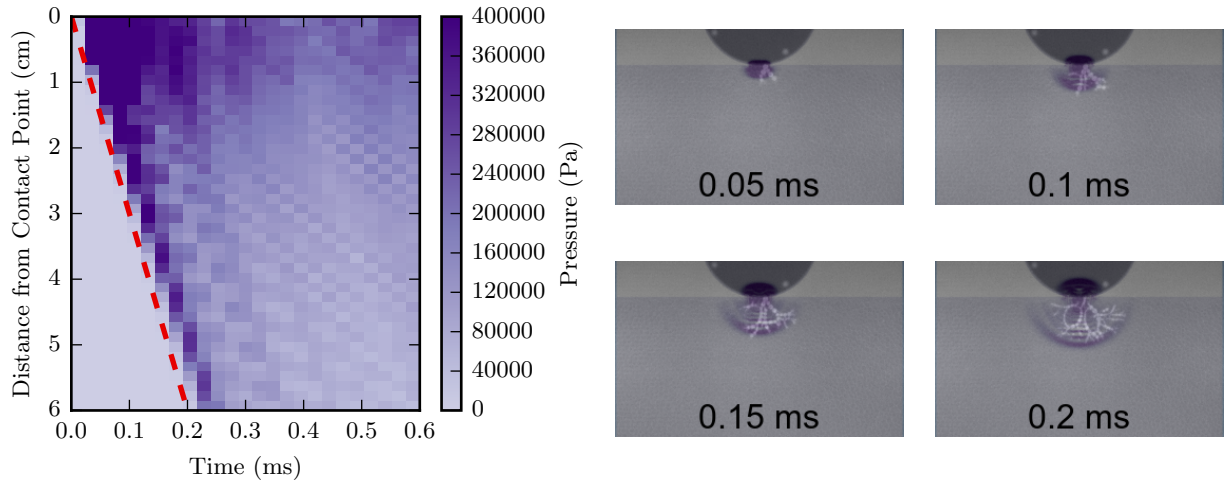

Figure 5: Stress/force propagation after intruder contact. Snapshots of the pressure at material points are overlaid on top of stills from the experimental movie found in the supplemental material of Clark et al. (2015) (right). The experimental data utilizes photoelasticity and shows stress-supporting particles in white color. We plot the pressure as a space-time plot (left) similar to that visualized in Clark et al. (2015). Dashed line corresponds to a speed of 300 m/s, the approximate front speed observed in the granular bulk in the cited work. All images share a common color scheme for the pressure, with dark purple indicating high pressure.

modulus of the intruder as low as possible. The intruder in this case consists of a bronze disc with diameter 12.7 cm and effective planar thickness 2.2 mm to match the results of Clark et al. (2015). It begins with an initial downward velocity of 5 meters per second. Although our intruder is bronze, we found that setting the Young's modulus of the intruder to a scant 20 MPa was sufficient – setting the modulus up to 1 GPa did not noticeably alter the results in the granular bulk. In line with the previous simulation, for the granular bulk we are considering the stiffest material, PS-1 from Vishay Precision Group. The parameters for this material remain unchanged from the previous section.

The simulation uses a 0.31m by 0.31m square grid discretized by 400 elements in each linear direction, and 9 total material points per filled element in the initial discretization. In total, over 400,000 material points were used to ensure precision; this number is much larger than needed if one utilizes a non-uniform grid and non-uniform initial particle placement, but suffices for our current purposes of demonstrating physical agreement. The time step size Δt is 0.15 μs, but we only needed to simulate the first 0.6 milliseconds. The total wall time taken by the simulation on an already-loaded Intel i5-3570k was approximately an hour and a half. The sampling rate of the output is set to 40 kHz to match the camera sampling rate in Clark et al. (2015).

We show snapshots of the propagating wave at specific times in the right half of fig. 5. The pressure of our simulation is overlaid atop the experiment, which utilized photoelastic disks so that particle forces can be correlated to light intensity. It can be seen that the pressure front models the force front observed experimentally. The figure on the left was made by considering the entire simulation and is intended to replicate the procedure done in Clark et al. (2015). First, all particles outside of a 90 degree sector symmetric about the vertical axis below the impact point are discarded. Next, particles are arranged in bins according to their radial distance from the impact point; the pressures from these particles are averaged. Each pressure value in a bin is shown by the color of a block, and each column in the image shows a snapshot in time of the average pressure at the radial distance indicated by the depth. Plotting the pressure versus depth and time in this way allows us to clearly visualize the propagating wave front and its speed. This apparent wave speed is compared to the theoretical p-wave speed of our material model (272 m/s) – as expected, these match quite well, and close to the experimentally observed range at around 300 m/s (indicated by a dashed line).

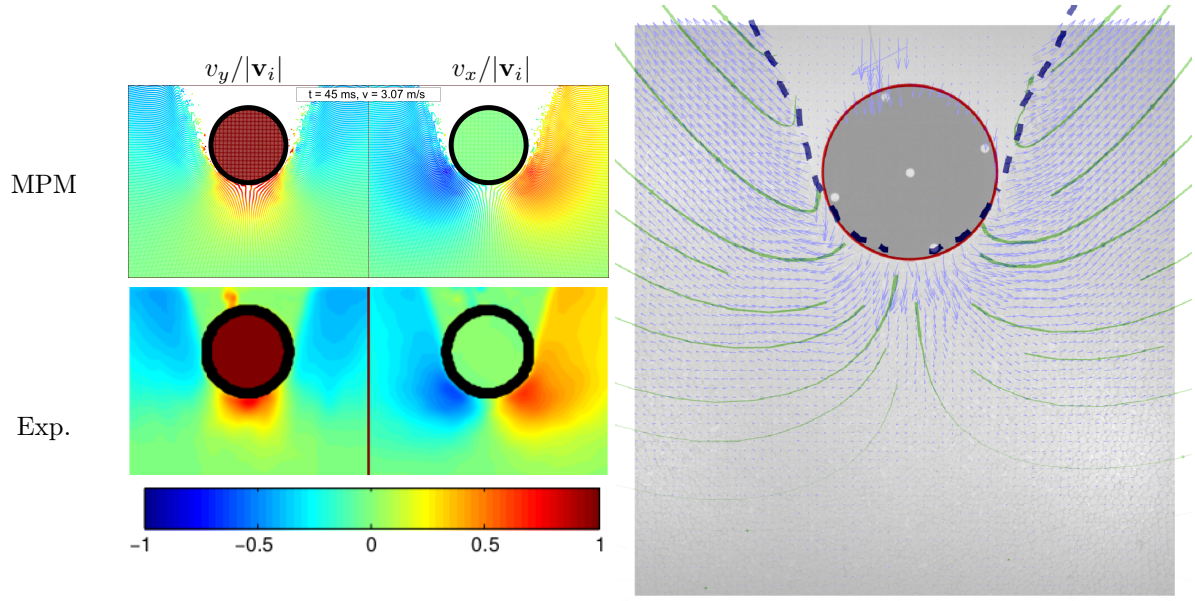

Figure 6: Comparison between the normalized granular velocity field from experimental results (left bottom, image taken from Clark (2014)) and those of the MPM simulation (left top). The velocity field is normalized against the intruder's center-of-mass velocity. The colorbar is common for all images; the left column shows the vertical component of normalized velocity, the right shows the horizontal component. Streamlines (MPM) and a coarse-grained velocity vector field plot (experiment) are shown as a further comparison (right). Simulation data was taken at 45 ms, which corresponds to an intruder velocity of $3.07\,\mathrm{m\,s^{-1}}$ (experimental data was taken when the intruder was traveling at $3.05\,\mathrm{m\,s^{-1}}$). Thicker streamlines indicate a higher velocity at that point. The computed free surface of the MPM simulation is shown via a dashed line.

4.3.2 Granular Bulk Motion

In addition to checking that forces (stresses) are propagated correctly, we also wished to check that the flow of the bulk was realistic. To this end, we extracted velocity fields underneath the intruder to compare to the data in Clark, Kondic, and Behringer (2016). We also compared the shape of the free surface of our method to a discrete element simulation performed in Seguin (2010). We switch to DEM simulations for the latter study because no free-surface or splash data was provided in the experimental studies.

Normalized Velocity Fields We continue to use the same bulk and intruder material properties as before, as these were unchanged in Clark, Kondic, and Behringer (2016) and that author's previous works. The intruder is a bronze disc with diameter 12.7 cm and is given an initial velocity of $5\,\mathrm{m\,s^{-1}}$. As in the prior simulations, we took the out-of-plane thickness to be 2.2 mm, whereas for the bulk the out-of-plane thickness is 3 mm, reducing the areal density by the appropriate factor. We show the values of the *nodal* velocity field as projected into the material point positions.

We observe good agreement in the velocity fields, as shown in fig. 6. Note the agreement is evident in both the magnitude and direction of the flow fields, as well as in the free surface shape in the intruder's wake, which is computed via a contour of the log of number density of material points at surrounding nodes. Interestingly, we also observed the type of "dynamic steady-state" phenomena described in Clark, Kondic, and Behringer (2016). Although the top left inset of fig. 6 was created when the intruder was still moving at $3.07\,\mathrm{m\,s^{-1}}$, the shape of the normalized velocity fields directly ahead the intruder appear nearly identical down to as low as $0.1\,\mathrm{m\,s^{-1}}$ with the circular intruder; naturally, the wake changes shape as material flows in behind the intruder, leading to differences in the velocity field in these regions.

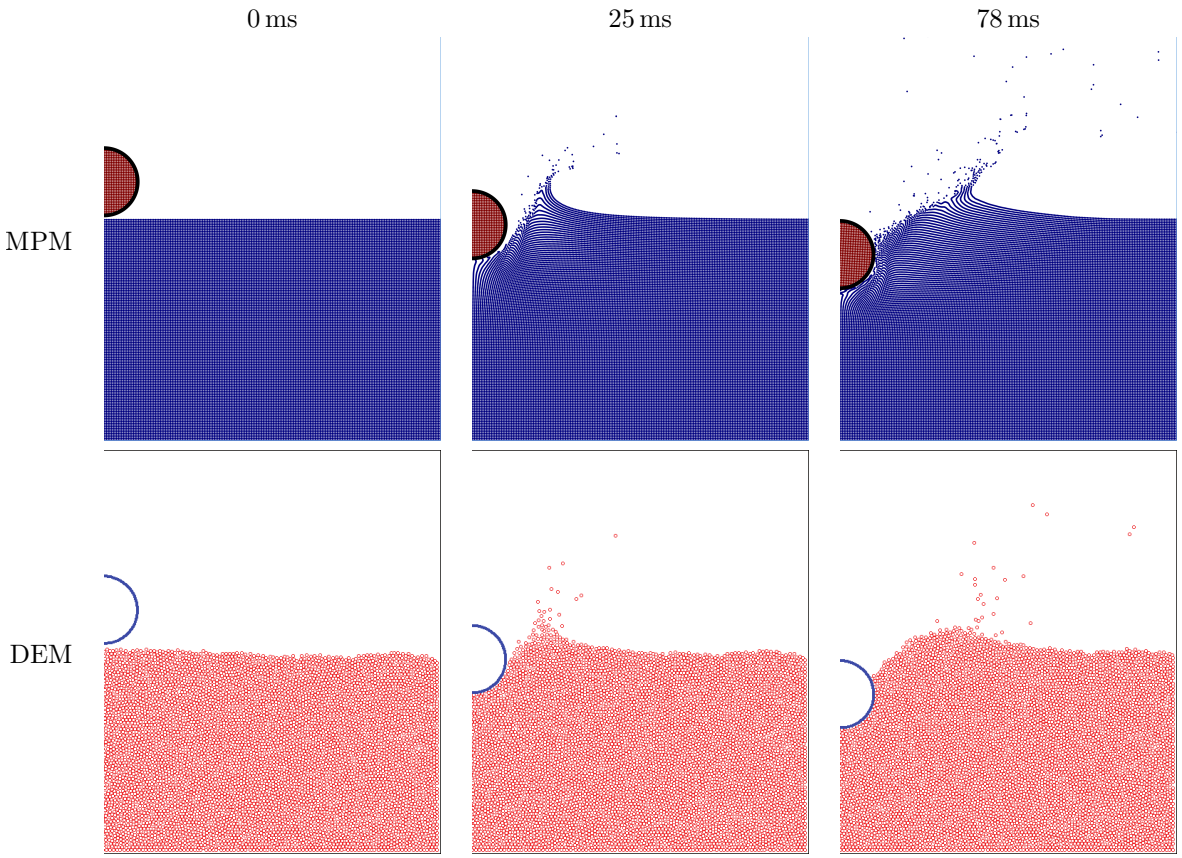

Figure 7: Comparison between an impact problem with DEM from Seguin (2010) (images taken from cited work, bottom row) and MPM (current work, top row). Snapshots are taken at 0, 25, and 78 milliseconds after the start of the simulation, which corresponds to the point in time where the intruder just touches the surface. For details on the bulk grain and intruder properties, see the main text.

Surface Shape Until this point, we have been using material properties calibrated to the grains from Clark, Petersen, and Behringer (2014); Clark et al. (2015); Clark, Kondic, and Behringer (2016). To verify the shape of free surface, we found results from a two-dimensional DEM simulation in Seguin (2010), which requires new material parameters.

The individual grains have diameter 1 mm, areal density $2500\,\mathrm{kg\,m^{-2}}$, and Young's Modulus 69 GPa. As the modulus of the bulk will be somewhat lower, we took this to be one tenth of the grain's modulus (6.9 GPa). Similarly, the packing fraction of these assemblies in two-dimensions is near 0.8, so we took the bulk areal density as $2000\,\mathrm{kg\,m^{-2}}$. Although no data was provided regarding a second elastic material property, we took the Poisson ratio to be 0.45 as before. For this simulation, the bulk material has dimensions 200 mm by 66 mm. The intruder has an identical density and identical elastic properties as an individual grains; only the diameter is different, which is given by 20 mm for the intruder. An interesting aspect of this DEM simulation is that no particle surface friction is used; following the results of Kamrin and Koval (2014), we know that this should correspond to a μ_s near 0.13, as we do not use the $\mu(I)$ relation with an exponential tail. In line with the cited work, we also take $\mu_2 = 0.428$ and $I_0 = 0.278$. Due to the frictionless nature of the DEM simulation, we used $\mu_{\mathrm{surf}} = 0$ (frictionless) contact between the intruder and the bulk.

A comparison of the DEM simulation from Seguin (2010) and the results from our MPM solver are shown in fig. 7; the surface shape progression is well-captured by the continuum method. In particular, we note that the splashing front of the two simulations sweep outward at similar rates and eject material at similar angles.

5 Conclusion

Using tabulated values for the granular bulk and a single penetration depth simulation for calibration of the unknown parameters, the continuum formulation presented is able to replicate, to a good level of agreement, a variety of experimental results pertaining to impact in a common material. We find that the penetration depths and flight time match the experimental data well. Force-like coefficients corresponding to terms in a dynamical equation for the position of the intruder were also recovered quantitatively. We verified that the elastodynamics are captured correctly by checking the p-wave speed in the granular bulk, and we also qualitatively see that the wavefront appears to develop similar spatial patterns as the experimental data. Also semi-quantitatively, the velocity fields of the granular bulk in the vicinity of the intruder appear to be closely matched with the coarse-grained velocity field obtained in experiment through particle image velocimetry; the dynamic steady state behavior was also observed in simulation during a large portion of the impact process. Lastly, using parameters for a different granular bulk material, the evolution of the free surface shape and material ejection when compared to a DEM simulation provides another validation. These results provide, to our knowledge, the first demonstration that a single granular continuum model is capable of representing the various aspects of granular impact.

From a numerical standpoint, we have noted improved behavior of the scheme presented in Dunatunga and Kamrin (2015) by using a variant of CPDI (itself a refinement of the original material point method) from Sadeghirad, Brannon, and Burghardt (2011) where the particle domain is fixed (similar to uGIMP). When combined with an improved contact algorithm from Huang et al. (2011), our simulation method was able to reliably implement continuum granular impact in true impact conditions, allowing the comparison to experimental results in both Clark, Petersen, and Behringer (2014) and Clark et al. (2015). The validity of the constitutive model and its numerical implementation in modeling many impact scenarios gives hope that the approach's validity is general to a potential array of granular flow problems, not limited by the possibility for a granular region to pass through the dense and disconnected phases.

6 Acknowledgements

This work was funded by grant NSF-CBET-1253228 and the MIT Department of Mechanical Engineering.

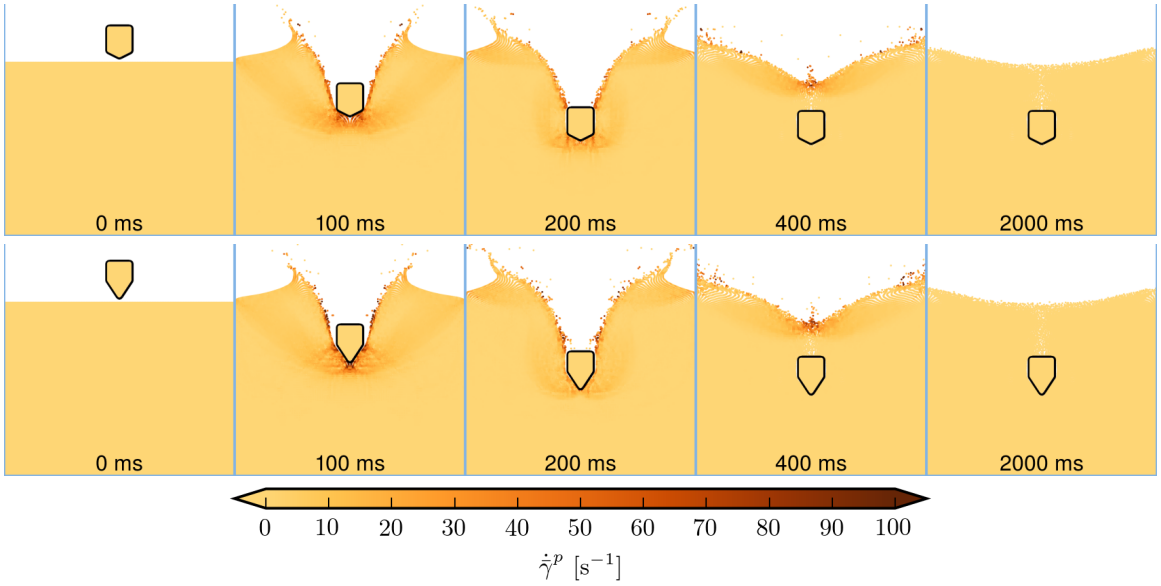

Figure 8: Here we show the equivalent plastic shear strain rate on a *linear* scale; the data is identical to that presented in fig. 2. It is a bit easier to notice that the strain rates are more concentrated towards the sharper intruder early on in the simulation, especially in the 100 ms image.

A Comparison to a Rate-Independent Model

As we noted in the main results, there is not much apparent dependence of the intruder motion on the μ_2 parameter in the $\mu(I)$ model. Indeed, for the dynamics of the intruder in this case, we can then presume that a rate independent model, such as that given by an elastic-perfectly plastic material with a Drucker-Prager yield criteron and non-associated flow rule, when combined with an appropriate density rule (to prevent tensile stress states and ratcheting), can capture the results almost as well as the rate dependent $\mu(I)$ rheology.

The rate-independent model then consists of a threshold for the stress ratio μ_s, below which the material acts as an elastic solid and at which any plastic strain rate is possible. Writing this as a condition on the equivalent shear stress results in the following form:

$$\bar{\tau} = \bar{\tau}(p, \dot{\bar{\gamma}}^p) = p\mu_s \quad \text{if} \quad \dot{\bar{\gamma}}^p > 0, \quad \text{and} \quad \bar{\tau} \leq p\mu_s \quad \text{if} \quad \dot{\bar{\gamma}}^p = 0. \tag{22}$$

Note that this can be easily implemented in the existing algorithm by simply setting μ_2 to μ_s, which eliminates the rate-dependent region in the $\mu(I)$ model, as seen by examining eq. (7).

To facilitate the comparison, we begin by showing plots of the equivalent plastic shear strain rate $\dot{\bar{\gamma}}^p$ (fig. 8) and inertial number I at material points for representative simulations in fig. 9. In line with Andersen and Andersen (2013), spatial smoothing of the pressure is employed for visualization here, by projecting from material points to nodes and then back to material points for plotting. Note that this is only done for visualization, and during simulation no such smoothing is employed.

We note that although the equivalent plastic shear strain rate is high underneath the intruder as shown in fig. 2 and fig. 8, so is the pressure, leading to only moderate I values nearly everywhere. This results in a strength which is only marginally higher than the lower bound given by μ_s.

Running a full set of simulations, we can generate the equivalent of fig. 3 using the rate-independent material. As the results are quite similar to that generated by the $\mu(I)$ model, we plot the results from the two models against each other in fig. 10. The most noticeable difference is that the rate-independent model predicts that the intruder has a larger depth and flight time compared to the $\mu(I)$ predictions and the experiments (refer back to fig. 3). This makes sense because the material is effectively weaker in the rate-independent model, because its resistance does not grow with flow rate. This may also explain why the difference is more noticeable when impact energy is larger.

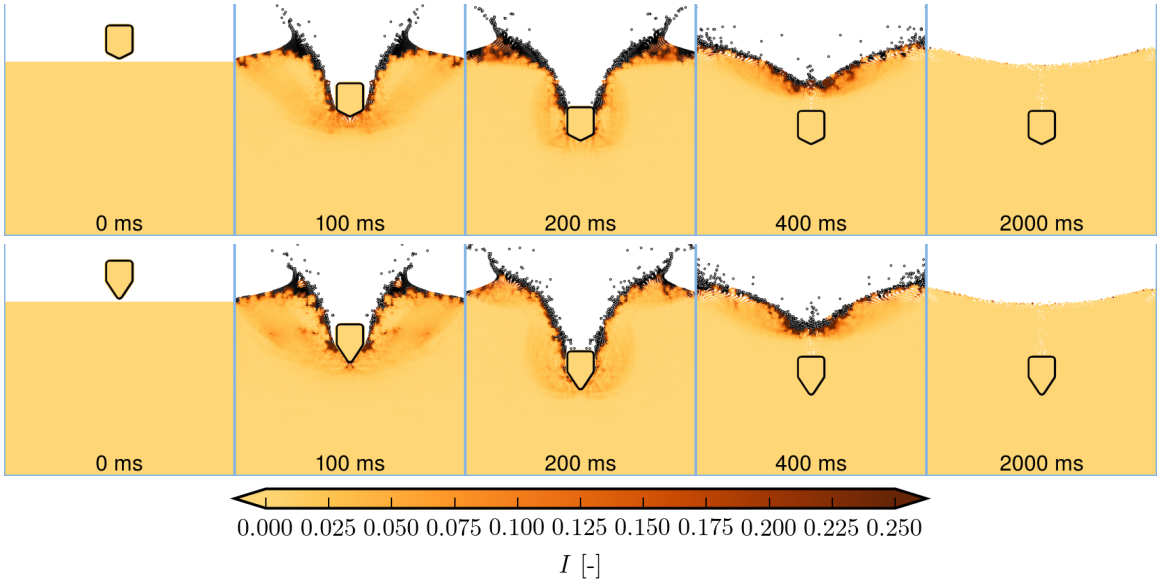

Figure 9: Here we plot the inertial number I using the same simulations as present in fig. 2. As open material has zero pressure, we have plotted these particles as open circles with black outlines. Note that the majority of the granular bulk is at a low inertial number; it is mostly the free surface, where the pressure is low, that exhibits higher I values. Although the strain rates are high underneath the intruder, as show in fig. 8, the pressure is also high in this region, leading to much smaller I values than may be initially expected. Together, these plots suggest that the level of rate-sensitivity for this problem will be low, except perhaps in the motion of the free surface. As a reference point, at $I = 0.1$, the strength of the material is given by $\mu \approx \tan 21.5$ degrees, whereas $\mu_s \approx \tan 17.75$ degrees.

Although there are only slight differences in this case, note that the plots of I indicate that the free surfaces may possess significantly different strengths than the bulk material; this in turn means that other impact situations may show a stronger effect with regards to rate-dependence, specifically where high equivalent plastic shear strain rates are not necessarily collocated with high pressures (e.g. if the projectile were to impact the granular media at an angle).

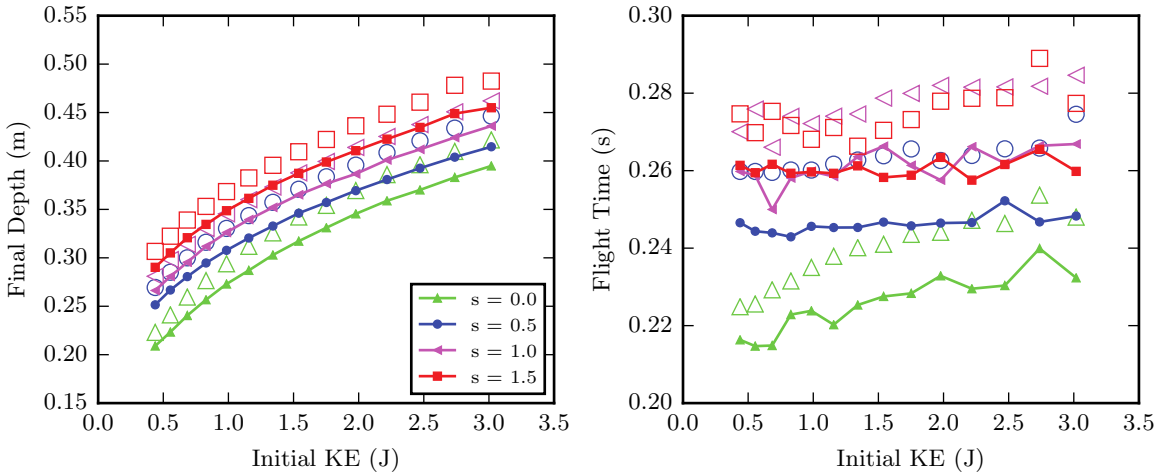

Figure 10: Final depth from the original surface of the bulk material (left) and the time until the intruder comes to a stop (right). Simulation results using the $\mu(I)$ model are represented by closed markers with connecting lines, while results using the rate-independent material are shown as open markers with no connecting line (the shape and colors correspond between the two sets of simulations, and are unchanged from the main text). As in the main text, final depth is taken to be the position at the end of 0.5 s, where all simulations appear to be entirely static. Similarly, as before stopping time calculated as the last time the intruder position is at most 0.2% of the total depth away from the final position. Note that the flight time of the rate-independent model appears to generally be higher (expected due to a lower average strength), but this does not seem to affect the final depth too much.

References

Abe, K., K. Soga, and S. Bandara. "Material Point Method for Coupled Hydromechanical Problems". *Journal of Geotechnical and Geoenvironmental Engineering* (2013), pp. 1–16.

Allen, W. A., E. B. Mayfield, and H. L. Morrison. "Dynamics of a projectile penetrating sand". *Journal of Applied Physics* 28.3 (1957), pp. 370–376.

Ambroso, M. A., R. D. Kamien, and D. J. Durian. "Dynamics of shallow impact cratering". *Phys. Rev. E* 72 (4 2005), p. 041305.

Andersen, S. and L. Andersen. "Analysis of stress updates in the material-point method". In: *Proceedings of the Twenty Second Nordic Seminar on Computational Mechanics*. Aalborg, 2009, pp. 129–134.

Andersen, S. and L. Andersen. *Post-Processing in the Material-Point Method*. Tech. rep. Aalborg: Aalborg University, 2013.

Bandara, S. and K. Soga. "Coupling of soil deformation and pore fluid flow using Material Point Method". *Computers and Geotechnics* 63 (2015), pp. 199–214.

Bardenhagen, S. G. and E. M. Kober. "The generalized interpolation material point method". *Computer Modeling in Engineering & Sciences* 5.6 (2004), pp. 477–495.

Bardenhagen, S. G. et al. "An Improved Contact Algorithm for the Material Point Method and Application to Stress Propagation in Granular Material". *Computer Modeling in Engineering & Sciences* 2.4 (2001), pp. 509–522.

Bathurst, R. and L. Rothenburg. "Micromechanical aspects of isotropic granular assemblies with linear contact interactions". *Journal of Applied Mechanics* 55.1 (1988), pp. 17–23.

Brackbill, J., D. Kothe, and H. Ruppel. "FLIP: A low-dissipation, particle-in-cell method for fluid flow". *Computer Physics Communications* 48 (1988), pp. 25–38.

Bruyn, J. R. de and A. M. Walsh. "Penetration of spheres into loose granular media". *Canadian Journal of Physics* 82.6 (2004), pp. 439–446. eprint: http://dx.doi.org/10.1139/p04-025.

Clark, A. H. and R. P. Behringer. "Granular impact model as an energy-depth relation". *EPL (Europhysics Letters)* 101.6 (2013), p. 64001.

Clark, A. H. "Granular Impact Dynamics: Grain Scale to Macroscale". PhD thesis. Duke University, 2014.

Clark, A. H., L. Kondic, and R. P. Behringer. "Particle Scale Dynamics in Granular Impact". *Phys. Rev. Lett.* 109 (23 2012), p. 238302.

Clark, A. H., L. Kondic, and R. P. Behringer. "Steady flow dynamics during granular impact". *Phys. Rev. E* 93 (5 2016), p. 050901.

Clark, A. H., A. J. Petersen, and R. P. Behringer. "Collisional model for granular impact dynamics". *Physical Review E* 89.1 (2014), p. 012201.

Clark, A. H. et al. "Nonlinear Force Propagation During Granular Impact". *Phys. Rev. Lett.* 114 (14 2015), p. 144502.

Cundall, P. A. and O. D. L. Strack. "A discrete numerical model for granular assemblies". *Geotechnique* 29.1 (1979), pp. 47–65.

Dunatunga, S. and K. Kamrin. "Continuum modelling and simulation of granular flows through their many phases". *Journal of Fluid Mechanics* 779 (Sept. 2015), pp. 483–513.

Farias, M., M. Llano-Serna, and J. Nairn. "Grid and time discretization issues affecting the application of the generalized material point method (GIMP) to simulate wedge penetration in soft soil". *Proceedings of New Frontiers in Computational Geotechnics (NFCOMGEO VI), Takayama, Japan, 21-23 May* (2012), pp. 1–8.

Furbish, D. J. et al. "Rain splash of dry sand revealed by high-speed imaging and sticky paper splash targets". *Journal of Geophysical Research: Earth Surface* 112.F1 (2007). F01001, n/a–n/a.

Gurtin, M. E., E. Fried, and L. Anand. *The mechanics and thermodynamics of continua*. Cambridge University Press, 2010.

Harlow, F. H. "The particle-in-cell computing method for fluid dynamics". *Methods in Computational Physics* 3.3 (1964), pp. 319–343.

Holsapple, K. A. "The Scaling of Impact Processes in Planetary Sciences". *Annual Review of Earth and Planetary Sciences* 21.1 (1993), pp. 333–373. eprint: http://dx.doi.org/10.1146/annurev.ea.21.050193.002001.

Housen, K. R. and K. A. Holsapple. "Impact cratering on porous asteroids". *Icarus* 163.1 (2003), pp. 102 –119.

Huang, P. et al. "Contact algorithms for the material point method in impact and penetration simulation". July 2010 (2011), pp. 498–517.

Jop, P., Y. Forterre, and O. Pouliquen. "A constitutive law for dense granular flows." *Nature* 441.7094 (June 2006), pp. 727–30.

Kamrin, K. and G. Koval. "Nonlocal Constitutive Relation for Steady Granular Flow". *Physical Review Letters* 108.17 (Apr. 2012), pp. 178301+.

Kamrin, K. and G. Koval. "Effect of particle surface friction on nonlocal constitutive behavior of flowing granular media". *Computational Particle Mechanics* 1.2 (2014), pp. 169–176.

Katsuragi, H. and D. J. Durian. "Unified force law for granular impact cratering". *Nature Physics* 3.6 (2007), pp. 420–423.

Kondic, L. et al. "Microstructure evolution during impact on granular matter". *Phys. Rev. E* 85 (1 2012), p. 011305.

Koval, G. et al. "Annular shear of cohesionless granular materials: From the inertial to quasistatic regime". *Physical Review E* 79.2 (Feb. 2009), p. 021306.

Lagrée, P.-Y., L. Staron, and S. Popinet. "The granular column collapse as a continuum: validity of a two-dimensional Navier–Stokes model with a μ(I)-rheology". *Journal of Fluid Mechanics* 686 (2011), pp. 378–408.

Mast, C. M. et al. "Simulating granular column collapse using the Material Point Method". *Acta Geotechnica* 10 (2015), pp. 101–116.

Melosh, H. J. *Impact cratering: A geologic process*. 1989.

Newhall, K. A. and D. Durian. "Projectile-shape dependence of impact craters in loose granular media". *Physical Review E* 68.6 (2003), p. 060301.

Royer, J. R. et al. "Birth and growth of a granular jet". *Phys. Rev. E* 78 (1 2008), p. 011305.

Sadeghirad, A., R. M. Brannon, and J. Burghardt. "A convected particle domain interpolation technique to extend applicability of the material point method for problems involving massive deformations". *International Journal for Numerical Methods in Engineering* 86.12 (2011), pp. 1435–1456.

Sadeghirad, A., R. M. Brannon, and J. E. Guilkey. "Second-order convected particle domain interpolation (CPDI2) with enrichment for weak discontinuities at material interfaces". July (2013), pp. 928–952.

Seguin, A. "De la pénétration en milieu granulaire". Theses. Université Paris Sud - Paris XI, Sept. 2010.

Silbert, L. E. et al. "Granular flow down an inclined plane: Bagnold scaling and rheology". *Physical Review E* 64.5 (2001), p. 051302.

Staron, L., P.-Y. Lagrée, and S. Popinet. "The granular silo as a continuum plastic flow: The hour-glass vs the clepsydra". *Physics of Fluids* 24.10 (2012), p. 103301.

Staron, L, P.-Y. Lagrée, and S Popinet. "Continuum simulation of the discharge of the granular silo: a validation test for the μ(I) visco-plastic flow law." *The European physical journal. E, Soft matter* 37.1 (Jan. 2014), p. 5.

Sulsky, D., Z. Chen, and H. L. Schreyer. "A particle method for history-dependent materials". *Computer Methods in Applied Mechanics and Engineering* 118.1-2 (Sept. 1994), pp. 179–196.

Sulsky, D. and A Kaul. "Implicit dynamics in the material-point method". *Computer Methods in Applied Mechanics and Engineering* 193.12-14 (Mar. 2004), pp. 1137–1170.

Tange, O. "GNU Parallel - The Command-Line Power Tool". *;login: The USENIX Magazine* 36.1 (2011), pp. 42–47.

Więckowski, Z. "Modelling of silo discharge and filling problems by the material point method". *Task Quarterly* 4.4 (2003), pp. 701–721.

Więckowski, Z. "The material point method in large strain engineering problems". *Computer Methods in Applied Mechanics and Engineering* 193.39-41 (Oct. 2004), pp. 4417–4438.

Więckowski, Z. and I. Kowalska-Kubsik. "Non-local approach in modelling of granular flow by the material point method". *Computer Methods in Mechanics* May (2011).

Zhao, R. et al. "Granular impact cratering by liquid drops: Understanding raindrop imprints through an analogy to asteroid strikes". *Proceedings of the National Academy of Sciences* 112.2 (2015), pp. 342–347. eprint: http://www.pnas.org/content/112/2/342.full.pdf.

da Cruz, F. et al. "Rheophysics of dense granular materials: Discrete simulation of plane shear flows". *Physical Review E* 72.2 (Aug. 2005), p. 021309.